Remote Sensing in Ecology and Conservation
Open Access
ZSL LET'S WORK FOR WILDLIFE

ORIGINAL RESEARCH

Semi-automated detection of eagle nests: an application of very high-resolution image data and advanced image analyses to wildlife surveys

Margaret E. Andrew & Jill M. Shephard

Environmental and Conservation Sciences, School of Veterinary and Life Sciences, Murdoch University, Murdoch, Western Australia, Australia

Keywords
eCognition, *Haliaeetus leucogaster*, image analysis, Maxent, nest surveys, object-based image analyses (OBIA), white-bellied sea eagle

Correspondence
Margaret E. Andrew, School of Veterinary and Life Sciences, Murdoch University, 90 South St., Murdoch WA 6150, Australia.
Tel: +61 8 9360 6121;
E-mail: m.andrew@murdoch.edu.au

Editor: Duccio Rocchini
Associate Editor: Graeme Buchanan

Received: 30 August 2016; Revised: 28 October 2016; Accepted: 6 December 2016

doi: 10.1002/rse2.38

Remote Sensing in Ecology and Conservation 2017;**3** (2):66–80

Abstract

Very high-resolution (VHR) image data, including from unmanned aerial vehicle (UAV) platforms, are increasingly acquired for wildlife surveys. Animals or structures they build (e.g. nests) can be photointerpreted from these images, however, automated detection is required for more efficient surveys. We developed semi-automated analyses to map white-bellied sea eagle (*Haliaeetus leucogaster*) nests in VHR aerial photographs of the Houtman Abrolhos Islands, Western Australia, an important breeding site for many seabird species. Nest detection is complicated by high environmental heterogeneity at the scale of nests (~1–2 m), the presence of many features that resemble nests and the variability of nest size, shape and context. Finally, the rarity of nests limits the availability of training data. These challenges are not unique to wildlife surveys and we show how they can be overcome by an innovative integration of object-based image analyses (OBIA) and the powerful machine learning one-class classifier Maxent. Maxent classifications using features characterizing object texture, geometry and neighborhood, along with limited object color information, successfully identified over 90% of high quality nests (most weathered and unusually shaped nests were also detected, but at a slightly lower rate) and labeled <2% of objects as candidate nests. Although this overestimates the occurrence of nests, the results can be visually screened to rule out all but the most likely nests in a process that is simpler and more efficient than manual photointerpretation of the full image. Our study shows that semi-automated image analyses for wildlife surveys are achievable. Furthermore, the developed strategies have broad relevance to image processing applications that seek to detect rare features differing only subtly from a heterogeneous background, including remote sensing of archeological remains. We also highlight solutions to maximize the use of imperfect or uncalibrated image data, such as some UAV-based imagery and the growing body of VHR imagery available in Google Earth and other virtual globes.

Introduction

Reliable estimates of population sizes are needed to support effective conservation and management of wildlife species. For example, several criteria within the IUCN Red List of Threatened Species rely on the size and trends of a species' global population (IUCN 2001). These estimates may be derived in a variety of ways, including direct counting of all or a sample of individuals within a population (e.g. Fuller et al. 1994), mark–recapture modeling (e.g. Meekan et al. 2006; Nicholson et al. 2012) or genetic analyses (e.g. Shephard et al. 2005a; Funk et al. 2012). For species exhibiting site fidelity during their life cycle, knowledge of these critical sites can help target locations for wildlife surveys. For example, population monitoring can be conducted at known seabird colonies (e.g. Fuller et al. 1994; Burbidge and Fuller 2004; Surman and Nicholson 2009) or sage grouse leks (e.g. Monroe et al. 2016). For species that do not form large aggregations, managers may track the number of breeding sites that are active (e.g. malleefowl mounds: Priddel and Wheeler 2003; bald eagle nests: Sauer et al. 2011; Watts

et al. 2008; Zwiefelhofer 2007) and evaluate breeding success at those sites.

Applications of image data to wildlife surveys

Remote sensing can support wildlife population surveys in several ways. First, counts of individual animals are increasingly made from very high-resolution (VHR) aerial photography, including imagery captured from unmanned aerial vehicle (UAV) platforms (e.g. Sardà-Palomera et al. 2012; Hodgson et al. 2013; Vermeulen et al. 2013; van Gemert et al. 2015). Although wildlife surveys have traditionally been conducted via direct observations, manual surveys are subjective; subject to observer bias, which can be extreme and unpredictable (Frederick et al. 2003); may involve hazardous conditions (Grier et al. 1981); or may be prohibitively expensive. Interpretation of aerial photos can help overcome some of the challenges of counting wildlife (Frederick et al. 2003; Trathan 2004), including improving population estimates, providing a documentary record and enabling the collection of additional information, such as animal spacing (Dolbeer et al. 1997) or orientation (Begall et al. 2008). In general, aerial photo-based wildlife surveys use manual photointerpretation (e.g. Anthony et al. 1995; Dolbeer et al. 1997; LaRue et al. 2011), which is time-consuming and remains subjective. Few objective, automated wildlife survey methods have been developed from image data, although Pettorelli et al. (2014) highlight that this is an emerging application for environmental remote sensing. Several semi-automated animal counting approaches have been advocated, largely relying on expert-determined brightness differences between the animals and their background (Gilmer et al. 1988), with pixels assembled into objects corresponding to individual animals after thresholding (Bajzak and Piatt 1990; Cunningham et al. 1996; Laliberte and Ripple 2003; Trathan 2004; Barber-Meyer et al. 2007). Such simple approaches may limit the capabilities of image-based wildlife surveys and are in stark contrast with the object-oriented approaches used to detect individual plants (but see Groom et al. 2011, 2013; Mejias et al. 2013; Witharana and Lynch 2016; Yang et al. 2014; and Abd-Elrahman et al. 2005 for a template matching approach).

Remote sensing can also detect breeding sites, at which more intensive monitoring may be performed. For example, breeding aggregations of penguins are detectable in satellite image data because their fecal matter stains the ice and snow (Fretwell and Trathan 2009; Witharana and Lynch 2016). Nest mounds of malleefowl have received considerable attention: techniques are under development to identify mound topography with lidar (Saffer and Peake 2014) or stereophoto (Thompson et al. 2015) data, and to evaluate mound activity with thermal imaging (Benshemesh and Emison 1996). Despite these examples (and see Butler 2002; Hughes et al. 2011; Puttock et al. 2015; Van Andel et al. 2015), remote detection of structures constructed by animals, such as nests, is less common than the detection and counting of animals themselves. The goal of this study was to develop semi-automated image processing tools to detect and map sea eagle nests from aerial photography.

Nest surveys of white-bellied sea eagles in the Houtman Abrolhos Islands

The white-bellied sea eagle (*Haliaeetus leucogaster*) is a charismatic species with cultural significance in Australasia. This species is fairly uniformly distributed around coastal Australia, and it also breeds at inland water bodies and offshore islands (Marchant and Higgins 1993; Shephard et al. 2005b). Information on the location of nests is fundamental for the management and conservation of sea eagles, including *H. leucogaster* in Australia and *H. leucocephalus* (bald eagle) in North America. Databases of nest locations are required for the monitoring and management of *H. leucogaster* in Tasmania, where it is strongly impacted by fisheries and forest management practices (Thurstans 2009a; Wiersma and Richardson 2009), as well as *H. leucocephalus* in the United States (Watts and Duerr 2010; Sauer et al. 2011). In addition, as eagles are especially sensitive to disturbances near their nests, conservation measures commonly protect buffers surrounding known nests (Dennis and Lashmar 1996; Dennis et al. 2011).

To date, aerial surveys with manual observers are the primary means for detecting and monitoring *Haliaeetus* nests (especially *H. leucocephalus*; e.g. Curnutt and Robertson 1994; Grier et al. 1981; Thurstans 2009b; Watts and Duerr 2010; Watts et al. 2008; Whitfield et al. 1974; Zwiefelhofer 2007). Eagle nests are large, conspicuous and maintained over a number of years; thus, they are amenable to aerial detection from surveys conducted at any time of year. However, there are no published accounts of attempts to detect and map sea eagle nests from image data, using either photointerpretation or image analyses.

We developed tools to detect eagle nests in VHR aerial photography of the Houtman Abrolhos Islands (HAI), nearly 200 islands and associated reefs 60 km offshore of Western Australia (Fig. 1). Islands in the HAI are small and of low elevation; the largest island has an area of 6.2 km^2 and the highest point on the islands is only 14 m above sea level (Department of Fisheries 2012). The HAI support nationally and regionally important breeding populations of seabirds, including the most significant

breeding habitat for *H. leucogaster* in the eastern Indian Ocean (Fuller et al. 1994; Department of Fisheries 2003). Monitoring seabirds on the HAI with traditional ground-based surveys is not a trivial job: with few exceptions, the islands are only accessible by sea and scattered over an area of 1000 km^2, separated by high seas and treacherous reefs. There are no permanent human residents on the HAI.

The detection of nests from image data of the HAI is more challenging than existing image-based approaches to survey wildlife. Many studies applying image analyses for wildlife surveys have taken advantage of simple systems with target species that are visually distinct from a featureless background (Groom et al. 2011; Trathan 2004; similarly, archeological remote sensing: Luo et al. 2014). In contrast, the surface characteristics of the HAI are *not* homogenous and many items in the background appear similar to nests in the aerial imagery, including drab vegetation and senescent plant matter. The nests themselves are heterogeneous and occur in diverse contexts. In contrast to elsewhere in the distribution of sea eagles, the HAI are not wooded, so the nests are constructed on the ground, on low shrubs or, rarely, within the canopy of mangroves. The nests may be formed as tall towers (Fig. 2A) or low matted areas atop seacliffs (Fig. 2B), occur singly or be surrounded by satellite nests and have immediate neighborhoods that vary in vegetation structure. The size and shape of seacliff nests in particular can vary considerably (Fig. 2B), and inconsistencies in the image data can contribute artifactual differences between nests on different islands. Finally, although sea eagles occur at higher densities on the HAI than on the mainland, few nests are available to train a classifier and they are spread across islands with different environmental characteristics and image acquisition conditions.

Given these challenges, it was necessary to develop a general nest detection algorithm that was robust to small sample sizes and variation in both nest characteristics and image acquisition parameters. The approach described here is likely to be relevant for any application to detect rare features that differ only subtly from a heterogeneous background, including wildlife surveys and detection of archeological remains (Luo et al. 2014; Lasaponara et al. 2016), or for rigorous analyses of uncalibrated image data, such as that available in Google Earth and other virtual globes (Johansen et al. 2008; Yu and Gong 2012).

Materials and Methods

Data

Field data

Nest surveys of selected islands of the HAI were conducted annually during 2012–2015. The nest surveys were timed to occur around the time of fledging (summer) when sea eagles are more tolerant of disturbances near

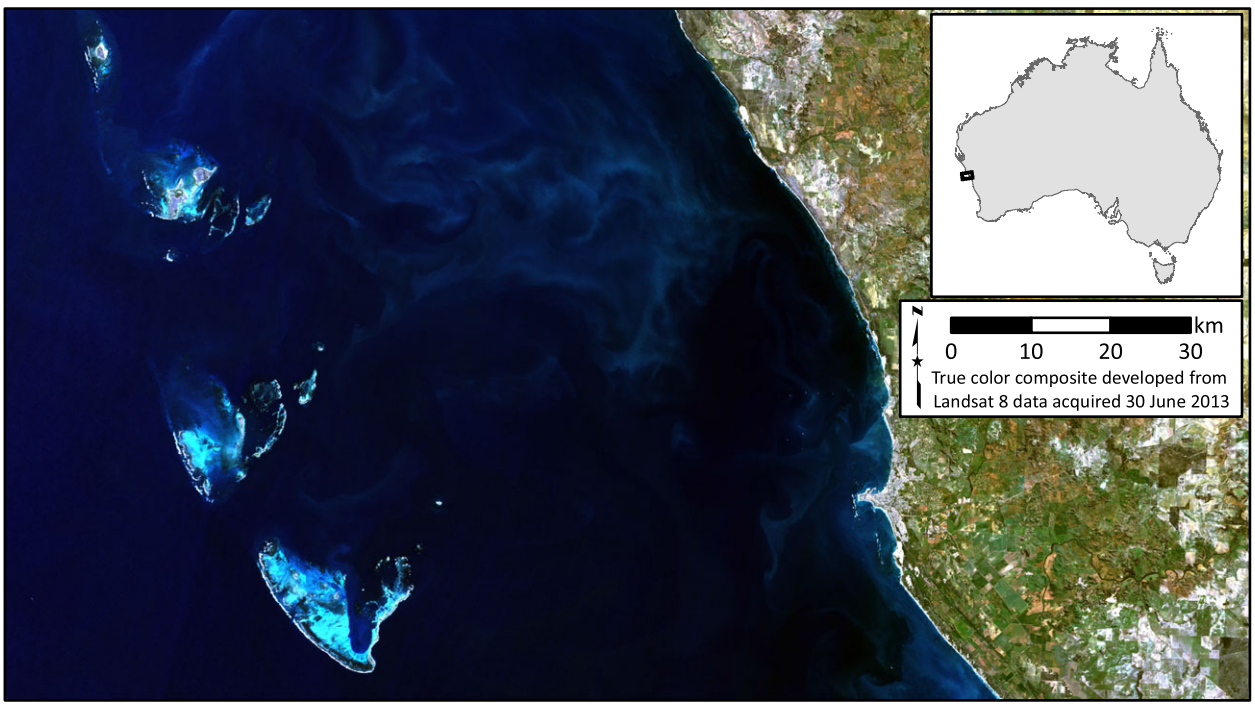

Figure 1. Locator map of the Houtman Abrolhos Islands, Western Australia.

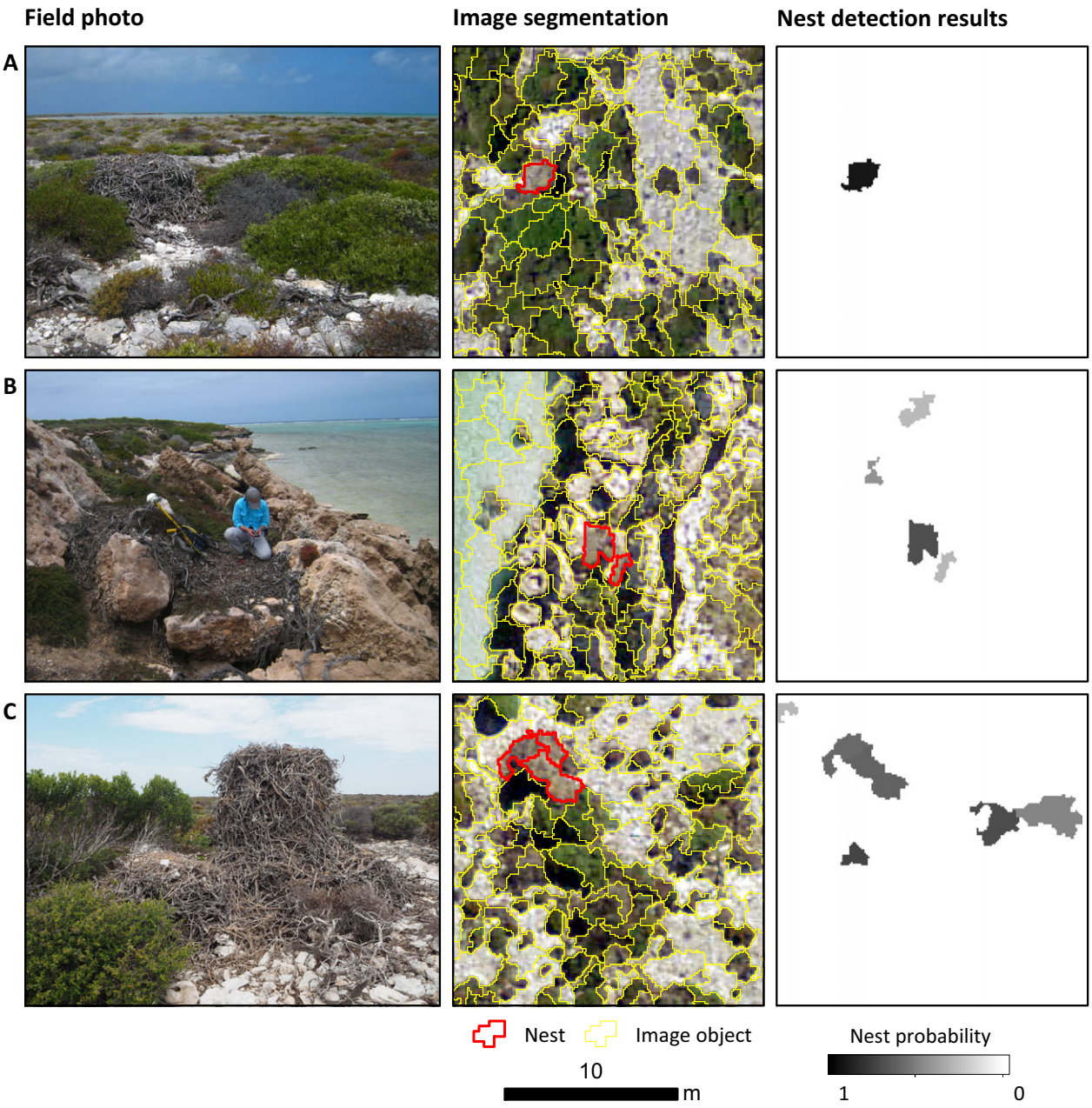

Figure 2. An illustration of three reference nests as they appear (*left*) in the field, (*center*) in the results of the image segmentation and (*right*) in the final results of the full nest detection analyses. In the final column, nests not meeting the classification threshold are omitted, and nests above the threshold are shaded by the continuous Maxent output they received to illustrate their relative degree of membership to the nest class. Nests illustrated include both (A) tower and (B) seacliff style sea eagle nests, and (C) a large osprey nest. In (B), JMS records characteristics of the main nest, while a satellite nest is present above and to her right. Field photo credits: (A,B) MEA, (C) D. Alpers. Base image reproduced by permission of the Western Australian Land Information Authority (Landgate) 2016.

the nest; however, nests with nestlings were not closely approached. The location of each observed nest was recorded with a differential GPS unit (Trimble Pro XRS or GeoXT, which each achieve submeter accuracy) and, where practical, photos of the nest (Fig. 2) were taken from each cardinal direction and from above. The nests were attributed to species – sea eagle (Fig. 2A and B) or osprey, *Pandion haliaetus* (Fig. 2C) – according to nest characteristics and the presence of feathers, pellets or nestlings. In total, 43 nests were recorded on nine islands;

33 were sea eagle nests, including three satellite nests near a main nest.

Aerial photography

Very high-resolution (10 cm pixels) true color aerial photography of the HAI were acquired on 23 April 2012 (northern island group) and 21 June–7 July 2012 (central and southern island groups), provided as a georeferenced (RMSE < 5 m) mosaic (www.landgate.wa.gov.au). Specific acquisition details for each image in the mosaic are unavailable and notable variation in illumination is evident, resulting in discrepancies in pixel values and image quality between images of different islands. There are no areas of overlap to enable image cross-calibration.

Image analyses

An object-based image analysis (OBIA) was pursued to detect sea eagle nests. OBIAs group contiguous pixels into objects, ideally corresponding to discrete entities in the image data, and apply a classification to the objects. OBIA is well suited to the VHR image data necessary for wildlife surveys. OBIA removes the requirement for absolute brightness differences between nests and background materials, which is unlikely to be met, instead requiring that discontinuities be present at nest edges. OBIAs also greatly expand the number and the type of variables available to distinguish nests from background materials, including differences in geometry, texture and relationships with the object's surroundings (Blaschke 2010). The full workflow is described below.

Preprocessing

Images of the nine islands containing observed nests were masked to the land area using a vector dataset of island boundaries (Department of Fisheries 2013) digitized from the same aerial photography used in this research. Because NIR data were not available, a vegetation index was estimated from the green and red bands: Red-Green NDVI, RGNDVI = (GREEN–RED)/(GREEN + RED). Although RGNDVI is less effective than the traditional NDVI, it provides a reasonable indicator of biophysical properties of the vegetation (Tucker 1979). Here, we use it as a general index of greenness, but note that it is fairly constrained in the HAI where several types of vegetation are not very green in the visible spectrum.

Images were then spatially filtered to remove extraneous pixel-to-pixel variation. To avoid blurring object boundaries, a multi-band edge preserving smoothing algorithm (following Laba et al. 2010) was coded and applied to the imagery in R (https://cran.r-project.org/). This approach evaluates the heterogeneity, averaged across all bands considered, of pixel values within petals surrounding the focal pixel. The average value of the petal with the least variability is selected as the new value for the focal pixel. This process was repeated 10 times, to allow the images to stabilize to final smoothed pixel values. Two bands were smoothed: the red band, which was found to have the best contrast of the original true color bands, and the RGNDVI. All image bands and products were scaled to range from 0 to 255.

Image segmentation and object features

Image objects were delineated at two hierarchical levels using eCognition's multi-resolution segmentation (Benz et al. 2004). This process iteratively builds objects of contiguous pixels, evaluating whether the addition of each pixel allows the object to maintain desired homogeneity and shape criteria, which are set by the user-defined 'scale' parameter (Trimble 2012). The scale parameter is an integrated measure of spectral and shape heterogeneity, and indirectly controls the size of the identified image objects. In general, larger scale parameters allow a greater level of heterogeneity, producing larger objects. Additional segmentation control parameters that contribute to the evaluation of the growing object include band weights, which set the relative importance of each of the provided image bands to the estimated spectral heterogeneity of the object; the shape weight, which determines the relative importance of object shape over spectral heterogeneity; and the compactness weight, which determines the preference for objects with compact versus complex shapes. The shape and compactness weights range from 0 to 1; higher values indicate greater importance of shape over spectral information in delineating the objects, and stronger preference for compact than complex object shapes, respectively (Trimble 2012).

Six image bands were used in the image segmentation: the original true color bands, RGNDVI and the smoothed red and RGNDVI bands. Segmentation was initially performed for a single island containing three nests with distinctive characteristics. For this image, segmentation parameters were adjusted iteratively to determine those most successful at delineating the known nests on this island. These segmentation parameters were refined slightly following evaluation on several additional islands. The final set of segmentation parameters (Table 1) was then applied to all images. Image objects were divided into subobjects to characterize their internal heterogeneity.

A variety of object features were calculated to characterize the image objects. Because of the inconsistent radiometry between islands, absolute color information or

brightness levels of the objects were not used. Instead, we extracted measures of the geometry, internal texture (calculated from the gray-level co-occurrence matrix, GLCM) and surrounding neighborhoods of objects (Table 2; and see Trimble 2012), which are expected to be transportable between islands, images and nest contexts, and should support robust, generic nest detection.

Maxent nest detection models, first pass

Nest objects were identified from the object features using the one-class maximum entropy classification (Maxent; Elith et al. 2011; Phillips et al. 2006; Phillips and Dudík 2008) with the Maxent software (Phillips et al. 2005). Maxent is a machine learning classification algorithm widely used in environmental studies and is among the best available algorithms for modeling species distributions (Elith et al. 2006). Its application to classification of remotely sensed data remains rare (Li and Guo 2010; Lin et al. 2014; Stenzel et al. 2014). However, it is an excellent choice for nest detection: Maxent makes no distributional assumptions, can model complex dependencies on the independent variables, including interactions between variables, performs well with low sample sizes and requires only presence data and a set of uncategorized background observations. Maxent estimates the probability distribution function of membership to the nest class along the supplied object features. From the set of viable solutions, it chooses the one that makes the fewest assumptions – that is most similar to the statistical distribution of the background objects (Elith et al. 2011). The logistic output of Maxent provides a continuous measure that is proportional to the probability that an object is a nest (Phillips and Elith 2013).

Several diagnostic outputs provide insights into the workings of Maxent. These diagnostics are measures of variable importance and variable response curves, which respectively highlight which object features make important contributions to the ability to discriminate nests and how nests differ from background objects along these features. We estimated variable importance as the percent reduction in model performance when a given variable is randomly permuted. Univariate response curves were created, plotting the logistic output for the observed values of each variable, without controlling for co-varying variables.

Models were built from a subset of 31 eagle nests from eight surveyed islands (data from the ninth island were used as independent test samples) randomly split into training (67%) and test (33%) nests, and a random set of 10,000 background objects, and applied to the full set of image objects. The results were calculated as the average of 10 replicate runs, each using unique training/test splits and different random background points. To avoid overfitting to the training nests, Maxent models were iteratively re-run, removing the least-important object feature at each step, until all included object features received importance estimates of >1%.

Table 1. eCognition parameters used to segment all images into objects and subobjects.

	Objects	Subobjects
Image bands and weights		
Red	2	2
Green	1	1
Blue	0	0
RGNDVI	5	5
Red, edge preserving smoothed	1	1
RGNDVI, edge preserving smoothed	1	1
Segmentation parameters		
Scale parameter	20	10
Shape (vs. color) weight	0.3	0.2
Compactness weight	0.75	0.5

Identifying dark bare surfaces and final Maxent models

Preliminary results suggested that it was not possible to efficiently detect nests without information about object color. Commission error rates were high, including objects that were clearly different shades than nests, and object features that incorporate some brightness information (e.g. GLCM mean) had high importance. To accommodate the absent image calibration causing inconsistent brightness values between images of different islands, we used outputs of an unsupervised pixel-level classification to provide some information about object color. ISODATA classifications were conducted on the three image bands and RGNDVI for each island. The desired number of output classes varied with island size and heterogeneity (range = [10, 50]). For the largest islands, given computing limitations, ISODATA classifications were developed on a random sample of 1% of pixels, which were used to train a maximum likelihood classifier applying the ISODATA results to the whole island. Classification results were manually screened to identify the classes capturing dark bare surfaces, the class comprising sea eagle nests, and produce a binary, pixel-level 'dark bare' layer. This product was imprecise and also captured much of the less-than-green vegetation, but contained information that was independent from the existing object features and provided helpful contrast between nests and surrounding objects in visual assessments. ISODATA classifications were performed in ENVI 5.1 (Harris Geospatial Solutions, Boulder, CO).

Table 2. Object features evaluated for their ability to discriminate between sea eagle nests and background image objects.

Object features	Description
Object color	
Dark bare fraction	Proportion of the pixels in an object assigned to the 'dark bare' class by a preliminary unsupervised classification
Object geometry	
Area	Number of pixels in an object
Length	An estimate of the length (long-axis) of an object, in pixels
Width	An estimate of the width (short-axis) of an object, in pixels
Asymmetry	An estimate of the shape complexity of the object, calculated from the variability of X and Y coordinates of pixels within the object
Compactness	An estimate of the shape complexity of the object, calculated as the ratio between the object's area and the area of a maximally compact object of the same dimensions
Elliptic fit	An estimate of the shape complexity of the object, calculated as the degree of fit between an object and a smooth ellipse of similar dimensions
Roundness	An estimate of the shape complexity of the object, calculated from the difference in size of ellipses that (1) completely enclose the object and (2) are completely enclosed by the object
Shape index	An estimate of the shape complexity of the object, calculated as the ratio between the object's perimeter and the perimeter of a maximally compact object of the same area
Object texture – pixel level	
Contrast, GLCM	Degree of contrast in brightness between neighbor pixels within an object; calculated in all directions for red band and RGNDVI
Entropy, GLCM	Evenness of cell values in the gray-level co-occurrence matrix; calculated in all directions for red band and RGNDVI
Mean, GLCM	Average pixel value, weighted by co-occurrence with other pixel values in the object; calculated in all directions for red band and RGNDVI
Correlation, GLCM	Spatial autocorrelation of pixel values within the object; calculated in all directions for red band and RGNDVI
Skewness	Describes the shape of the statistical distribution of pixel values within the object
Object texture – subobject level	
Number of subobjects	The number of subobjects contained within the object
Subobject variability	Standard deviation of pixel values within subobject, averaged across all subobjects in the object; calculated for red band and RGNDVI
Subobject area	Average area of subobjects in the object
Subobject area variability	Standard deviation of areas of the subobjects within the object
Subobject shape	Asymmetry of subobjects, averaged across all subobjects in the object
Subobject shape variability	Standard deviation of asymmetries of the subobjects within the object
Object neighborhood	
Mean difference to neighbors	An estimate of the contrast between the object and its neighborhood, measured as the difference between the object's average pixel value and the average pixel value of the neighboring objects; calculated for red band, RGNDVI and the dark bare fraction
Standard deviation to neighbors	An estimate of the immediate neighborhood of an object, measured as the variability of pixel values in the bounding box surrounding an object; calculated for red band, RGNDVI and the dark bare class
Number of neighbors	The number of objects adjoining the object's border

Pixel-level texture metrics were calculated from the gray-level co-occurrence matrix (GLCM) following Haralick et al. (1973).

Several other researchers have found that coarse pixel-level classification outputs provide useful inputs to OBIAs (Yang et al. 2014; Lasaponara et al. 2016), however, they included the classification results among the layers used to derive the segmentation. In contrast, we retained the image objects produced as described in the section 'Image segmentation and object features,' but estimated new object features using the dark bare layer: the fraction of an object in the dark bare class, and characteristics of the object's neighborhood in this layer (Table 2).

A final set of replicate Maxent runs was performed including the new dark bare measures. We also refined the training data used: (1) Background objects were constrained to the set of objects receiving Maxent predictions within the range of values assigned to true nests in the first pass models. (2) Only a set of 23 'high quality' nests were used. The eight nests excluded from these models were heavily weathered discarded nests, unrepresentative nests (e.g. the single nest in a mangrove) or poorly segmented into objects.

A difficulty with one-class classifiers such as Maxent is the selection of a threshold value to transform the continuous output to a binary classification result (Mack et al. 2014). In order to be conservative and avoid missing many nests, we set the threshold at the output value corresponding to an omission rate on the training nests of 10%, averaged across the 10 replicate runs.

Validation

Classification performance was evaluated using the area under the receiver operating characteristic (ROC) curve (AUC), estimated on the 33% of hold-out nests for each replicate Maxent run. AUC values >0.5 indicate classifier performance better than random; AUC > 0.7 indicates a useful model. In addition, detection rates are reported for both the set of 23 high-quality sea eagle nests and the remaining 20 nests not used in the final Maxent models. The detection rate of high quality nests is likely an optimistic estimate since each nest was used to train, on average, two-thirds of the replicate runs. However, detection of the 20 independent nests is probably a conservative estimate. Although two of these nests are sea eagle nests from the independent test island, the remainder are osprey nests (often distinctly taller than sea eagle nests; Fig. 2C), or sea eagle nests deemed to be unrepresentative and excluded from the final Maxent models (as described above).

Results

The image segmentation produced over 2 million objects across the nine islands and was generally successful at delineating known nests (Fig. 2, central column). However, it was difficult to determine a set of generic segmentation parameters optimized for all images and nests. A few nests were subdivided into several objects (e.g. Fig. 2C) and/or included surrounding areas within the main nest object, although this did not necessarily preclude the Maxent classifiers from identifying these nests.

Although the first pass of Maxent models were insufficient, they successfully excluded ~83% of all image objects that were extremely unlikely to be nests, achieving AUC = 0.94 on the hold-out set of test nests, averaging across the 10 replicates. Thirteen object features were retained following stepwise removal of unimportant variables (Table 3). The most important object features for distinguishing nests, in this pass, characterized object relationships with its neighborhood and texture, although size – both area and the linear dimensions of length and width – also made contributions (Table 3). Nests tended to occur in pixel neighborhoods with modest, but not zero, variability in greenness, and were less green than neighboring objects (Fig. 3). In addition, nests had medium to dark brightness values in the red band, when weighted by the co-occurrence of values between adjacent pixels (GLCM mean), extremely low internal pixel-to-pixel contrast in the red band and had similar shades in the red band to neighboring objects (Fig. 3). The likelihood of being a nest peaked for objects that had an area of ~500 pixels (5 m^2), and that were roughly 20 pixels (2 m) across (Fig. 3).

The dark bare classification results substantially improved the nest detection models, reducing the set of possible nests to 1.9% of all image objects when using the average 10% training omission threshold. AUC values for the final Maxent models were slightly lower than in the first pass (AUC = 0.87), likely because only the set of 'tough cases' were used as background objects for training

Table 3. Importance of object features at distinguishing between sea eagle nests and background objects in both the first pass and final Maxent models.

Object features	First pass Maxent	Final Maxent
Object color		
Dark bare fraction	—	**18.20**
Object geometry		
Area	**10.87**	7.10
Length	6.24	2.00
Width	4.98	5.11
Compactness	—	1.89
Roundness	3.12	—
Object texture – pixel level		
Contrast, GLCM; red band	**11.60**	3.74
Contrast, GLCM; RGNDVI	2.29	—
Entropy, GLCM; RGNDVI	1.58	—
Mean, GLCM; red band	**13.56**	—
Mean, GLCM; RGNDVI	—	3.19
Correlation, GLCM, red band	—	1.29
Skewness, green band	2.15	—
Skewness, blue band	—	1.62
Object texture – subobject level		
Subobject area variability	—	1.04
Object neighborhood		
Mean diff to neighbors, red band	6.99	—
Mean diff to neighbors, RGNDVI	**16.80**	—
Mean diff to neighbors, dark bare fraction	—	**21.19**
Standard deviation to neighbors, red band	3.61	—
Standard deviation to neighbors, RGNDVI	**16.17**	**25.06**
Standard deviation to neighbors, dark bare fraction	—	6.74
Number of neighbors	—	1.80

Variable importance was estimated by permutation. Values shown are the average across 10 replicate runs for both Maxent models. Values in bold indicate variables with above-average importance.

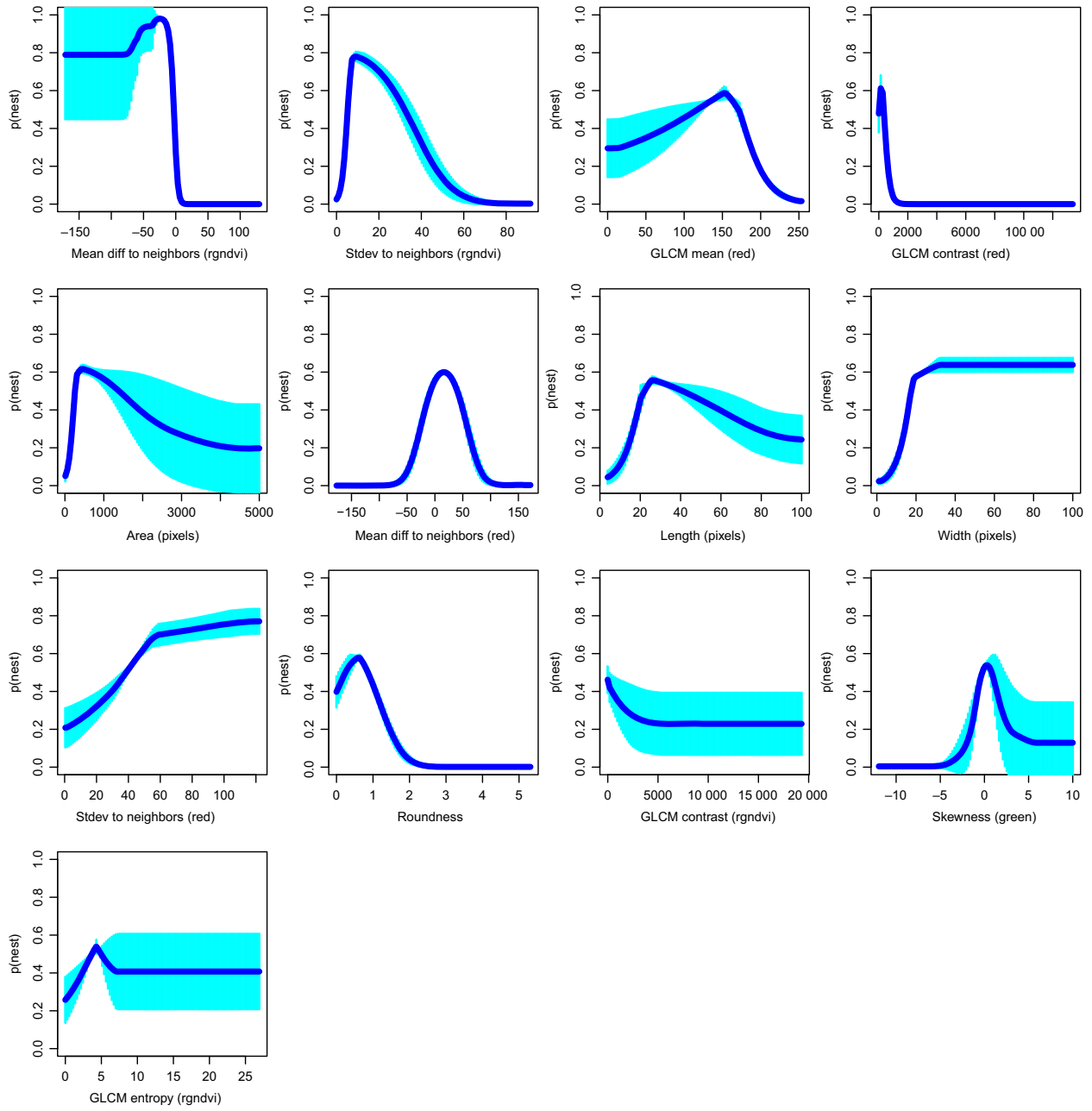

Figure 3. Univariate response curves from the first pass Maxent classification, illustrating the relationships between evaluated object features and predicted probability of nest membership. Graphs plot the mean ± standard deviation (shading) of 10 replicate Maxent runs for all variables retained in the models. Object features are ordered by decreasing variable importance.

and evaluation. The detection rate of the averaged final Maxent predictions on the 'high quality' nests was 91% (21 of 23 nests). The model was also reasonably successful at identifying independent, poor quality nests, with a detection rate of 75%: nine out of 20 nests were successfully detected; another six, three of them large, ramshackle osprey nests, were missed but adjacent objects of nest debris were successfully classified as nests.

There were 14 object features in the final Maxent models (Table 3). Interestingly, the most important feature was the variability of greenness in the object neighborhood, which was the second most important feature in the first pass Maxent models (Table 3). Other object features with high importance in the final Maxent models were those derived from the dark bare classification results (Table 3). The likelihood of being a nest increased

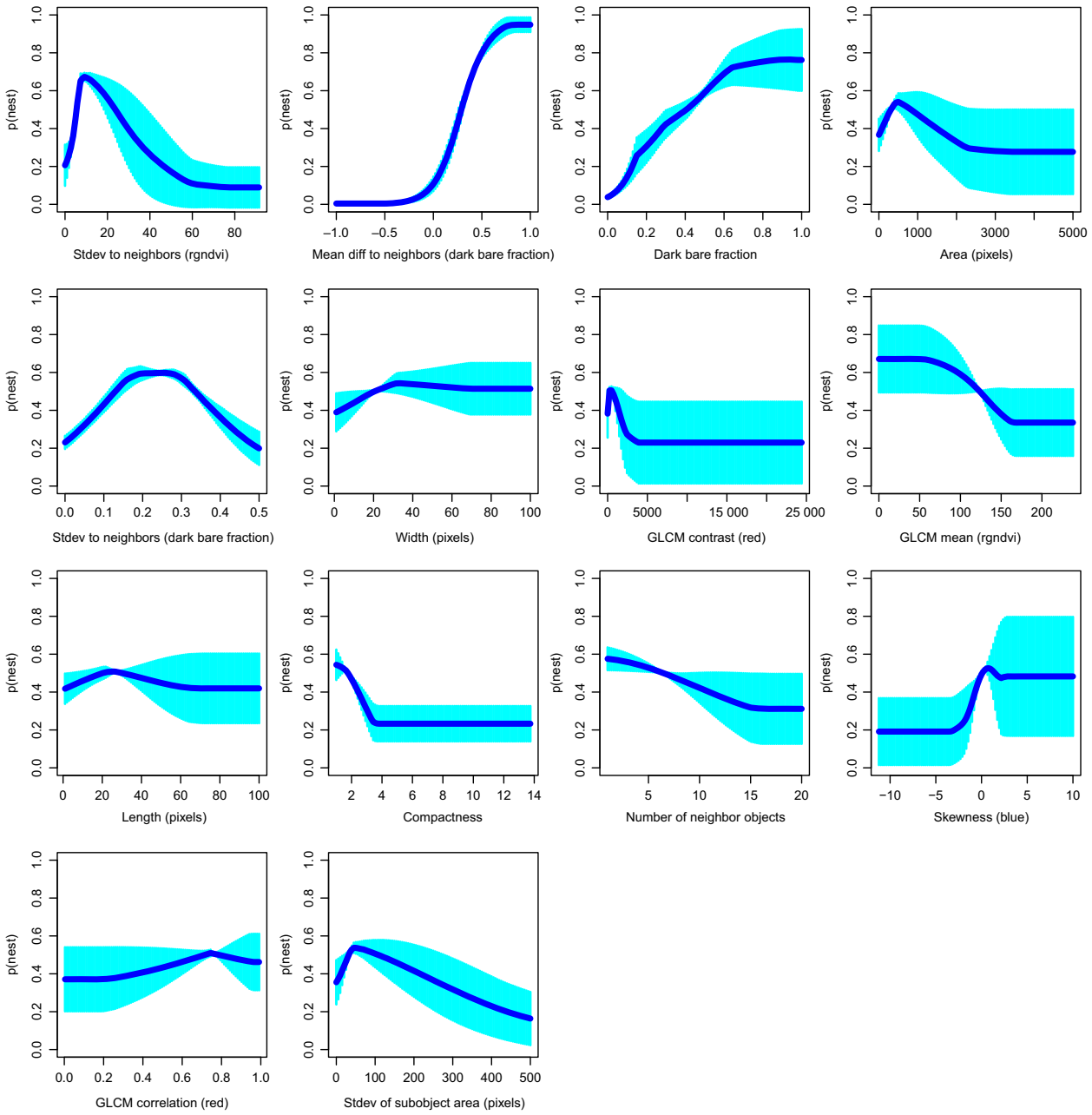

Figure 4. Univariate response curves from the final Maxent classification. Graphs plot the mean ± standard deviation (shading) of 10 replicate Maxent runs for all variables retained in the models. Object features are ordered by decreasing variable importance.

as the fraction of dark bare pixels within an object increased; nests also had a higher fraction of dark bare pixels than their neighbors, and tended to occur in neighborhoods with moderate pixel-level variability in the dark bare layer (Fig. 4). In addition, several variables that featured prominently in the first pass models maintained their importance and exhibited similar response curves (Table 3; Fig. 4).

The nest detection results are mapped out in Figure 2 (right column) for a diverse selection of nests, including both tower (Fig. 2A) and seacliff (Fig. 2B) style sea eagle nests of varying size and shape, and a large osprey nest (Fig. 2C). In addition, the segmentation and classification results in Figure 2B and C give an indication of what some of the false positive cases surrounding the known nests are like.

Discussion

Despite the considerable challenges of detecting rare, subtle objects against a heterogeneous background, we demonstrate that it is possible to identify sea eagle nests from very high-resolution aerial photography using advanced image analyses. The semi-automated nest detection analyses presented here correctly detected over three-quarters of all nests and labeled <2% of the features occurring on the islands as candidate nests. Of the sample of reference nests, 91% of high quality nests were identified, and the majority of an independent set of weathered, unusual or poorly segmented nests were also detected. While nests certainly do not make up 2% of the island area, a high over-prediction rate is likely unavoidable given the lack of strong discriminating features between nests and many of the other natural occurring objects on the islands and wide variation in nest characteristics in the image data, both due to physical differences between the nests and differences in image acquisition. Thus, the performance of the automated nest detection analyses is extremely positive. Our results are comparable to Mejias et al. (2013), who also report high false positive rates for their automated detections of dugongs from UAV-based photography.

Although the results over-predict the occurrence of nests, they are suitable to guide nest inventories, monitoring and management of this species. The mapped results can be visually screened by a natural resource manager to rule out all but the most likely nests. This process is much simpler and more efficient than manually photointerpreting nests from the full image. Many of the nests are ambiguous in aerial imagery and easy to overlook (see, e.g. the sample of nests illustrated in Fig. 2). Manual search of the full images for nests is an uncertain, draining process that would probably not achieve the high detection rates (75–91%) of the semi-automated analyses. In contrast, it is much simpler to screen the candidate nest objects identified by the semi-automated analyses to determine whether or not they are likely to be true nests. This is for several reasons; (1) it is a much more bounded task: as humans, it is easier to decide whether or not a specific image object, from those selected by the Maxent models, is likely to be an actual nest, than to perform an open-ended search of the entire images to discern the subtle features related to nests; (2) although OBIA are often framed as being more similar to the human process of photointerpretation than are pixel-level analyses, the Maxent models here are obviously using additional and complementary information to the cues we use in visual interpretation. As a result, many of the objects identified as candidate nests by the models are quite distinct from true nests to the analyst, and can be discarded from the candidate set very quickly.

The successful detection of sea eagle nests was enabled by the creative integration of object-based image analyses and a powerful machine learning classifier. The advantages of OBIA are clear: the spatial characteristics of image objects add a wealth of independent information that improve the detectability of items of interest. OBIA have been successfully applied to a range of objectives, including the detection of subtle features such as isolated tree mortality within forests (Guo et al. 2007), seismic lines (He et al. 2011) and archeological remains (Luo et al. 2014; Lasaponara et al. 2016), and are beginning to be evaluated for wildlife surveys (Groom et al. 2011, 2013; Yang et al. 2014). However, many OBIA examples to date use rule-based expert system classifiers, in part because they are easily implemented in the popular eCognition software. While *a priori* decision rules work well in many contexts, they may limit the capabilities of OBIA when the target differs subtly from background objects; is distinguishable along features that are not readily intuitive, such as the gray-level co-occurrence matrix (GLCM) texture metrics; or is separable due to complex multivariate interactions between object features, but not in straightforward univariate comparisons.

Although we are pleased with the performance of the semi-automated nest detection and believe that the results are suitable to guide management, there is likely room for improvement within the developed workflow. First, the requirement for a single set of segmentation parameters limited the ability to successfully delineate all nests into image objects. It is not possible to give absolute recommendations about the segmentation parameters most appropriate for a given goal. The parameters in eCognition are indirectly related to the size and characteristics of ensuing objects, and optimal settings vary depending on the characteristics of the image data and the environment being imaged (Moffett and Gorelick 2013). If a sample of known reference nests exists in all images to be analyzed, it may be possible to optimize the segmentation individually for each island, but this reduces the ease of transferring this method between islands with somewhat comparable image data.

Other gains may be achieved by increasing the amount of information gleaned from both classifications that were performed. The intermediary ISODATA classification results contributed crucial advances to our ability to discriminate sea eagle nests by allowing the final Maxent classification to make some use of the color of the objects, which was otherwise unreliable due to the lack of calibration between images. Waser et al. (2011) also found that color information improved individual tree species classifications over those developed using object geometry alone. However, we took relatively little advantage of the ISODATA results, deriving a single broad class

expected to be directly related to the nests: pixels similar in color to dark bare ground. Yet, a number of other clusters related to other surface features were produced, which may contain additional useful information for characterizing nests and the relationships between nests and their neighborhoods.

Finally, it may be possible to reduce commission error rates with a full classification, rather than a one-class classifier. One-class classifiers are attractive because they remove the need to have adequate training data for classes that are not of interest (Lin et al. 2014; Stenzel et al. 2014). However, without reference data for other classes, appropriate thresholds to create a final binary output cannot be objectively determined, especially when there is considerable similarity between the target and other classes (Mack et al. 2014). With a one-class classifier, all that is known is that a given object may have high similarity to the target, whereas a full classifier may reveal that, nevertheless, the object is more similar to another class, reducing the area assigned to the target class. An effective compromise may be the approach of Stenzel et al. (2014), who mapped four classes simultaneously with Maxent, allowing the identification of pixels with ambiguous estimates of class membership.

It may seem that a poor choice of image data created many unnecessary difficulties for our study. Nest detection may be improved by the availability of NIR data, facilitating discrimination of nests from drab vegetation, and would be simplified by the use of calibrated image data, enabling direct use of color information. However, we consider these disadvantages of our data and the solutions we devised to overcome them to be a strength of this study. Wildlife managers and environmental practitioners often have little control over the spatial data available to them and must make the most of imperfect data. The limitations of our aerial photography – no calibration and true color bands only – are common and likely to become more so given the emergence of non-traditional data sources such as some UAV-based imagery and the VHR image mosaics in Google Earth and other virtual globes. Virtual globes are an immense resource, as the high-resolution imagery they contain would not otherwise be freely available. However, due to their scant metadata and uncertain radiometry, standard pixel-level analyses of such data are inappropriate (Yu and Gong 2012). Consequently, Google Earth imagery is most often interpreted manually (e.g. Begall et al. 2008; Dorais and Cardille 2011; Hughes et al. 2011; Visser et al. 2014; Westcott and Andrew 2015). However, while absolute pixel values may not be reliable, the relationships between neighboring pixels are, and image texture and object-based analyses, such as those described here, of the imagery within virtual globes can support rigorous research and diverse applications (Barbier et al. 2010; Mering et al. 2010; Ploton et al. 2012; Luo et al. 2014). Olea and Mateo-Tomás (2016) complain that virtual globes are currently underused by ecologists. The insights of our nest detection analyses and our workflow are broadly applicable, and we hope they will stimulate researchers and practitioners to get more out of non-traditional image data, for wildlife surveys and beyond.

Acknowledgements

This research was funded by the National Geographic Society's Committee for Research and Exploration grant #9545-14. The field surveys would not have been possible without the generous support of the Western Australia Department of Fisheries. N. Dunlop (Conservation Council of Western Australia), D. Alpers, R. Phillips and A. Frost also provided valuable assistance in the field.

Data Accessibility

A data table of the estimated features for all image objects is archived in Andrew (2016; doi:10.6084/m9.figshare.4502486).

References

Abd-Elrahman, A., L. Pearlstine, and F. Percival. 2005. Development of pattern recognition algorithm for automatic bird detection from unmanned aerial vehicle imagery. *Surveying Land Inf. Sci.* **65**, 37–45.

Anthony, R. M., W. H. Anderson, J. S. Sedinger, and L. L. McDonald. 1995. Estimating populations of nesting brant using aerial videography. *Wildl. Soc. Bull.* **23**, 80–87.

Bajzak, D., and J. F. Piatt. 1990. Computer-aided procedure for counting waterfowl on aerial photographs. *Wildl. Soc. Bull.* **18**, 125–129.

Barber-Meyer, S. M., G. L. Kooyman, and P. J. Ponganis. 2007. Estimating the relative abundance of emperor penguins at inaccessible colonies using satellite imagery. *Polar Biol.* **30**, 1565–1570.

Barbier, N., P. Couteron, C. Proisy, Y. Malhi, and J. P. Gastellu-Etchegorry. 2010. The variation of apparent crown size and canopy heterogeneity across lowland Amazonian forests. *Glob. Ecol. Biogeogr.* **19**, 72–84.

Begall, S., J. Červený, J. Neef, O. Vojtěch, and H. Burda. 2008. Magnetic alignment in grazing and resting cattle and deer. *Proc. Natl Acad. Sci. USA* **105**, 13451–13455.

Benshemesh, J. S., and W. B. Emison. 1996. Surveying breeding densities of malleefowl using an airborne thermal scanner. *Wildl. Res.* **23**, 121–142.

Benz, U. C., P. Hofmann, G. Willhauck, I. Lingenfelder, and M. Heynen. 2004. Multi-resolution, object-oriented fuzzy analysis of remote sensing data for GIS-ready information. *ISPRS J. Photogramm. Remote Sens.* **58**, 239–258.

Blaschke, T. 2010. Object based image analysis for remote sensing. *ISPRS J. Photogramm. Remote Sens.* **65**, 2–16.

Burbidge, A. A., and P. J. Fuller. 2004. Numbers of non-burrowing breeding seabirds of the Houtman Abrolhos: 1991-1993 and 1999. *Corella* **28**, 96–103.

Butler, D. R. 2002. Visualizing animal impacts on the landscape: remote sensing in the geography classroom. *Geocarto Int.* **17**, 69–76.

Cunningham, D. J., W. H. Anderson, and R. M. Anthony. 1996. An image-processing program for automated counting. *Wildl. Soc. Bull.* **24**, 345–346.

Curnutt, J. L., and W. B. Robertson. 1994. Bald eagle nest-site characteristics in south Florida. *J. Wildl. Manage.* **58**, 218–221.

Dennis, T. E., and A. F. C. Lashmar. 1996. Distribution and abundance of white-bellied sea-eagles in South Australia. *Corella* **20**, 93–102.

Dennis, T. E., R. R. McIntosh, and P. D. Shaughnessy. 2011. Effects of human disturbance on productivity of white-bellied sea-eagles (*Haliaeetus leucogaster*). *Emu* **111**, 179–185.

Department of Fisheries. 2003. Inventory of the land conservation values of the Houtman Abrolhos Islands, Fisheries Management Paper No. 151. Perth, Western Australia: Department of Fisheries.

Department of Fisheries. 2012. *Exploring the Houtman Abrolhos Islands*. Department of Fisheries, Perth, Western Australia.

Department of Fisheries. 2013. *Coastline - Abrolhos Islands*. Department of Fisheries, Perth, Western Australia.

Dolbeer, R. A., J. L. Belant, and G. E. Bernhardt. 1997. Aerial photography techniques to estimate populations of laughing gull nests in Jamaica Bay, New York, 1992-1995. *Colonial Waterbirds* **20**, 8–13.

Dorais, A., and J. Cardille. 2011. Strategies for incorporating high-resolution Google Earth databases to guide and validate classifications: understanding deforestation in Borneo. *Remote Sens.* **3**, 1157–1176.

Elith, J., C. H. Graham, R. P. Anderson, M. Dudík, S. Ferrier, A. Guisan, et al. 2006. Novel methods improve prediction of species' distributions from occurrence data. *Ecography* **29**, 129–151.

Elith, J., S. J. Phillips, T. Hastie, M. Dudík, Y. E. Chee, and C. J. Yates. 2011. A statistical explanation of maxent for ecologists. *Divers. Distrib.* **17**, 43–57.

Frederick, P. C., B. Hylton, J. A. Heath, and M. Ruane. 2003. Accuracy and variation in estimates of large numbers of birds by individual observers using an aerial survey simulator. *J. Field Ornithol.* **74**, 281–287.

Fretwell, P. T., and P. N. Trathan. 2009. Penguins from space: faecal stains reveal the location of emperor penguin colonies. *Glob. Ecol. Biogeogr.* **18**, 543–552.

Fuller, P. J., A. A. Burbidge, and R. Owens. 1994. Breeding seabirds of the Houtman Abrolhos, Western Australia 1991-1993. *Corella* **18**, 97–113.

Funk, W. C., J. K. McKay, P. A. Hohenlohe, and F. W. Allendorf. 2012. Harnessing genomics for delineating conservation units. *Trends Ecol. Evol.* **27**, 489–496.

van Gemert, J. C., C. R. Verschoor, P. Mettes, K. Epema, L. P. Koh, and S. Wich. 2015. Nature conservation drones for automatic localization and counting of animals. *Lect Notes Comput Sc.* **8925**, 255–270.

Gilmer, D. S., J. A. Brass, L. L. Strong, and D. H. Card. 1988. Goose counts from aerial photographs using an optical digitizer. *Wildl. Soc. Bull.* **16**, 204–206.

Grier, J. W., J. M. Gerrard, G. D. Hamilton, and P. A. Gray. 1981. Aerial-visibility bias and survey techniques for nesting bald eagles in northwestern Ontario. *J. Wildl. Manage.* **45**, 83–92.

Groom, G., I. K. Petersen, M. D. Anderson, and A. D. Fox. 2011. Using object-based analysis of image data to count birds: mapping of lesser flamingos at Kamfers Dam, Northern Cape, South Africa. *Int. J. Remote Sens.* **32**, 4611–4639.

Groom, G., M. Stjernholm, R. D. Nielsen, A. Fleetwood, and I. K. Petersen. 2013. Remote sensing image data and automated analysis to describe marine bird distributions and abundances. *Ecol. Inform.* **14**, 2–8.

Guo, Q. H., M. Kelly, P. Gong, and D. S. Liu. 2007. An object-based classification approach in mapping tree mortality using high spatial resolution imagery. *GISci. Remote Sen.* **44**, 24–47.

Haralick, R. M., K. Shanmuga, and I. Dinstein. 1973. Textural features for image classification.*IEEE Transactions on Systems Man and Cybernetics* **SMC-3**, 610–621.

He, Y. H., S. E. Franklin, X. L. Guo, and G. B. Stenhouse. 2011. Object-oriented classification of multi-resolution images for the extraction of narrow linear forest disturbance. *Remote Sen. Let.* **2**, 147–155.

Hodgson, A., N. Kelly, and D. Peel. 2013. Unmanned aerial vehicles (UAVs) for surveying marine fauna: a dugong case study. *PLoS ONE* **8**, e79556.

Hughes, B. J., G. R. Martin, and S. J. Reynolds. 2011. The use of Google Earth (TM) satellite imagery to detect the nests of masked boobies *Sula dactylatra*. *Wildlife Biol.* **17**, 210–216.

IUCN. 2001. *IUCN Red List Categories and Criteria version 3.1*. Gland, Switzerland and Cambridge, UK: IUCN Species Survival Commission. IUCN.

Johansen, K., C. Roelfsema, and S. Phinn. 2008. Preface: High spatial resolution remote sensing for environmental monitoring and management. *J. Spatial Sci.* **53**, 43–47.

Laba, M., B. Blair, R. Downs, B. Monger, W. Philpot, S. Smith, et al. 2010. Use of textural measurements to map invasive wetland plants in the Hudson River National Estuarine Research Reserve with IKONOS satellite imagery. *Remote Sens. Environ.* **114**, 876–886.

Laliberte, A. S., and W. J. Ripple. 2003. Automated wildlife counts from remotely sensed imagery. *Wildl. Soc. Bull.* **31**, 362–371.

LaRue, M. A., J. J. Rotella, R. A. Garrott, D. B. Siniff, D. G. Ainley, G. E. Stauffer, et al. 2011. Satellite imagery can be used to detect variation in abundance of Weddell seals (*Leptonychotes weddellii*) in Erebus Bay, Antarctica. *Polar Biol.* **34**, 1727–1737.

Lasaponara, R., G. Leucci, N. Masini, R. Persico, and G. Scardozzi. 2016. Towards an operative use of remote sensing for exploring the past using satellite data: the case study of Hierapolis (Turkey). *Remote Sens. Environ.* **174**, 148–164.

Li, W. K., and Q. H. Guo. 2010. A maximum entropy approach to one-class classification of remote sensing imagery. *Int. J. Remote Sens.* **31**, 2227–2235.

Lin, J. Y., X. P. Liu, K. Li, and X. Li. 2014. A maximum entropy method to extract urban land by combining MODIS reflectance, MODIS NDVI, and DMSP-OLS data. *Int. J. Remote Sens.* **35**, 6708–6727.

Luo, L., X. Y. Wang, H. D. Guo, C. S. Liu, J. Liu, L. Li, et al. 2014. Automated extraction of the archaeological tops of qanat shafts from VHR imagery in Google Earth. *Remote Sens.* **6**, 11956–11976.

Mack, B., R. Roscher, and B. Waske. 2014. Can I trust my one-class classification? *Remote Sens.* **6**, 8779–8802.

Marchant, S., and P. Higgins. 1993. *Handbook of Australian, New Zealand and Antarctic Birds* Vol. **3**. Oxford University Press, Melbourne.

Meekan, M. G., C. J. A. Bradshaw, M. Press, C. McLean, A. Richards, S. Quasnichka, et al. 2006. Population size and structure of whale sharks *Rhincodon typus* at Ningaloo Reef, Western Australia. *Mar. Ecol. Prog. Ser.* **319**, 275–285.

Mejias, L., G. Duclos, A. Hodgson, and F. Maire. 2013. Automated marine mammal detection from aerial imagery. *Proceedings of OCEANS '13 IEEE/MTS*.

Mering, C., J. Baro, and E. Upegui. 2010. Retrieving urban areas on Google Earth images: application to towns of West Africa. *Int. J. Remote Sens.* **31**, 5867–5877.

Moffett, K. B., and S. M. Gorelick. 2013. Distinguishing wetland vegetation and channel features with object-based image segmentation. *Int. J. Remote Sens.* **34**, 1332–1354.

Monroe, A. P., D. R. Edmunds, and C. L. Aldridge. 2016. Effects of lek count protocols on greater sage-grouse population trend estimates. *J. Wildl. Manage.* **80**, 667–678.

Nicholson, K., L. Bejder, S. J. Allen, M. Krützen, and K. H. Pollock. 2012. Abundance, survival and temporary emigration of bottlenose dolphins (*Tursiops* sp.) off Useless Loop in the western gulf of Shark Bay, Western Australia. *Marine Freshwater Res.* **63**, 1059–1068.

Olea, P. P., and P. Mateo-Tomás. 2016. Exploiting virtual globes for ecology and conservation in the digital earth era. *Front. Ecol. Environ.* **14**, 11–12.

Pettorelli, N., W. F. Laurance, T. G. O'Brien, M. Wegmann, H. Nagendra, and W. Turner. 2014. Satellite remote sensing for applied ecologists: opportunities and challenges. *J. Appl. Ecol.* **51**, 839–848.

Phillips, S. J., and M. Dudík. 2008. Modeling of species distributions with maxent: new extensions and a comprehensive evaluation. *Ecography* **31**, 161–175.

Phillips, S. J., and J. Elith. 2013. On estimating probability of presence from use-availability or presence-background data. *Ecology* **94**, 1409–1419.

Phillips, S. J., M. Dudík, and R. E. Schapire. 2005. Maxent software for species habitat modeling, version 3.3.3k. https://www.cs.princeton.edu/~schapire/maxent/ (Accessed 12 July 2013).

Phillips, S. J., R. P. Anderson, and R. E. Schapire. 2006. Maximum entropy modeling of species geographic distributions. *Ecol. Model.* **190**, 231–259.

Ploton, P., R. Pélissier, C. Proisy, T. Flavenot, N. Barbier, S. N. Rai, et al. 2012. Assessing aboveground tropical forest biomass using Google Earth canopy images. *Ecol. Appl.* **22**, 993–1003.

Priddel, D., and R. Wheeler. 2003. Nesting activity and demography of an isolated population of malleefowl (*Leipoa ocellata*). *Wildl. Res.* **30**, 451–464.

Puttock, A. K., A. M. Cunliffe, K. Anderson, and R. E. Brazier. 2015. Aerial photography collected with a multirotor drone reveals impact of Eurasian beaver reintroduction on ecosystem structure. *J. Unmanned Vehicle Sys.* **3**, 123–130.

Saffer, V., and T. Peake. 2014. The use of LiDAR to determine the presence of Malleefowl mounds. Proceedings of the 5th National Malleefowl Forum, 140-150.

Sardà-Palomera, F., G. Bota, C. Viñolo, O. Pallarés, V. Sazatornil, L. Brotons, et al. 2012. Fine-scale bird monitoring from light unmanned aircraft systems. *The Ibis* **154**, 177–183.

Sauer, J. R., M. C. Otto, W. L. Kendall, and G. S. Zimmerman. 2011. Monitoring bald eagles using lists of nests: response to Watts and Duerr. *J. Wildl. Manage.* **75**, 509–512.

Shephard, J. M., J. M. Hughes, C. P. Catterall, and P. D. Olsen. 2005a. Conservation status of the white-bellied sea-eagle *Haliaeetus leucogaster* in Australia using mtDNA control region sequence data. *Conserv. Genet.* **6**, 413–429.

Shephard, J. M., C. P. Catterall, and J. M. Hughes. 2005b. Long-term variation in the distribution of the white-bellied sea-eagle (*Haliaeetus leucogaster*) across Australia. *Austral Ecol.* **30**, 131–145.

Stenzel, S., H. Feilhauer, B. Mack, A. Metz, and S. Schmidtlein. 2014. Remote sensing of scattered Natura 2000 habitats using a one-class classifier. *Int. J. Appl. Earth Obs. Geoinf.* **33**, 211–217.

Surman, C. A., and L. W. Nicholson. 2009. A survey of the breeding seabirds and migratory shorebirds of the Houtman Abrolhos, Western Australia. *Corella* **33**, 81–98.

Thompson, S., G. Thompson, J. Sackmann, J. Spark, and T. Brown. 2015. Using high-definition aerial photography to search in 3D for malleefowl mounds is a cost-effective alternative to ground searches. *Pac. Conserv. Biol.* **21**, 208–213.

Thurstans, S. D. 2009a. A survey of white-bellied sea-eagle *Haliaeetus leucogaster* nests in Tasmania in 2003. *Corella* **33**, 66–70.

Thurstans, S. D. 2009b. Modelling the nesting habitat of the white-bellied sea-eagle *Haliaeetus leucogaster* in Tasmania. *Corella* **33**, 51–65.

Trathan, P. N. 2004. Image analysis of color aerial photography to estimate penguin population size. *Wildl. Soc. Bull.* **32**, 332–343.

Trimble. 2012. *eCognition Developer 8.8 Reference Book*. Trimble Germany GmbH, Munchen, Germany.

Tucker, C. J. 1979. Red and photographic infrared linear combinations for monitoring vegetation. *Remote Sens. Environ.* **8**, 127–150.

Van Andel, A. C., S. A. Wich, C. Boesch, L. P. Koh, M. M. Robbins, J. Kelly, et al. 2015. Locating chimpanzee nests and identifying fruiting trees with an unmanned aerial vehicle. *Am. J. Primatol.* **77**, 1122–1134.

Vermeulen, C., P. Lejeune, J. Lisein, P. Sawadogo, and P. Bouché. 2013. Unmanned aerial survey of elephants. *PLoS ONE* **8**, e54700.

Visser, V., B. Langdon, A. Pauchard, and D. M. Richardson. 2014. Unlocking the potential of Google Earth as a tool in invasion science. *Biol. Invasions* **16**, 513–534.

Waser, L. T., C. Ginzler, M. Kuechler, E. Baltsavias, and L. Hurni. 2011. Semi-automatic classification of tree species in different forest ecosystems by spectral and geometric variables derived from airborne digital sensor (ADS40) and RC30 data. *Remote Sens. Environ.* **115**, 76–85.

Watts, B. D., and A. E. Duerr. 2010. Nest turnover rates and list-frame decay in bald eagles: implications for the national monitoring plan. *J. Wildl. Manage.* **74**, 940–944.

Watts, B. D., G. D. Therres, and M. A. Byrd. 2008. Recovery of the Chesapeake Bay bald eagle nesting population. *J. Wildl. Manage.* **72**, 152–158.

Westcott, F., and M. E. Andrew. 2015. Spatial and environmental patterns of off-road vehicle recreation in a semi-arid woodland. *Appl. Geogr.* **62**, 97–106.

Whitfield, D. W. A., J. M. Gerrard, W. J. Maher, and D. W. Davis. 1974. Bald eagle nesting habitat density and reproduction in central Saskatchewan and Manitoba. *Canadian Field-Naturalist* **88**, 399–408.

Wiersma, J., and A. Richardson. 2009. Foraging of white-bellied sea-eagles *Haliaeetus leucogaster* in relation to marine fish farms in Tasmania. *Corella* **33**, 71–79.

Witharana, C., and H. J. Lynch. 2016. An object-based image analysis approach for detecting penguin guano in very high spatial resolution satellite images. *Remote Sens.* **8**, 375.

Yang, Z., T. J. Wang, A. K. Skidmore, J. de Leeuw, M. Y. Said, and J. Freer. 2014. Spotting East African mammals in open savannah from space. *PLoS ONE* **9**, e115989.

Yu, L., and P. Gong. 2012. Google Earth as a virtual globe tool for Earth science applications at the global scale: progress and perspectives. *Int. J. Remote Sens.* **33**, 3966–3986.

Zwiefelhofer, D. 2007. Comparison of bald eagle (*Haliaeetus leucocephalus*) nesting and productivity at Kodiak National Wildlife Refuge, Alaska, 1963-2002. *J. Raptor Res.* **41**, 1–9.

